AIP ADVANCES **5**, 053205 (2015)

Thermal conductance of superlattice junctions

Simon Lu and Alan J. H. McGaughey[a]
Department of Mechanical Engineering, Carnegie Mellon University, Pittsburgh, Pennsylvania 15213, USA

(Received 31 January 2015; accepted 3 April 2015; published online 14 April 2015)

We use molecular dynamics simulations and the lattice-based scattering boundary method to compute the thermal conductance of finite-length Lennard-Jones superlattice junctions confined by bulk crystalline leads. The superlattice junction thermal conductance depends on the properties of the leads. For junctions with a superlattice period of four atomic monolayers at temperatures between 5 and 20 K, those with mass-mismatched leads have a greater thermal conductance than those with mass-matched leads. We attribute this lead effect to interference between and the ballistic transport of emergent junction vibrational modes. The lead effect diminishes when the temperature is increased, when the superlattice period is increased, and when interfacial disorder is introduced, but is reversed in the harmonic limit. [http://dx.doi.org/10.1063/1.4918591]

I. INTRODUCTION

Semiconductor superlattice nanostructures have received considerable research attention since their first appearance in the 1970s.[1,2] They have applications in solid state lighting and thermoelectric energy conversion due to the size-tunability of their electronic properties. Within a light-emitting diode, lattice-assisted electron-hole recombination generates heat, which must be adequately dissipated in order to maintain performance and prolong device life. The possibility of tuning superlattice design for low thermal conductivity provides a potential path to optimizing the thermoelectric figure of merit.

Early experimental measurements of superlattices revealed that their thermal conductivities were reduced from the bulk thermal conductivities of their constituent materials.[3–5] This finding was attributed to (i) reduction of phonon mean free paths within the layers and (ii) thermal resistance at the internal interfaces. Computational work on thermal transport within superlattices has been performed using equilibrium[6,7] and non-equilibrium[6,8–13] molecular dynamics (MD) simulations. MD studies are limited by classical statistics and are performed on systems for which empirical potentials are available [e.g., Lennard-Jones (LJ) argon, Stillinger-Weber Si-Ge, and Tersoff graphene-BN]. Work has also been done using perturbative anharmonic lattice dynamics calculations, using force constants from both analytical potentials and from density functional theory calculations.[14–16]

A minimum in superlattice thermal conductivity with superlattice period length was predicted using a simple theoretical model by Simkin and Mahan,[17] observed computationally using both MD and lattice-based computational techniques,[6,11,12,18] and recently observed experimentally by Ravichandran *et al*.[19] This minimum is described as a consequence of the transition between a regime where vibrational wave interference significantly affects thermal transport (i.e., the coherent regime) and a regime where waves do not interfere and a particle-like treatment is appropriate.[17]

Since superlattices in technological applications are typically grown on substrates and are finite in length, they differ significantly from the ideal infinite superlattice. Instead, it is appropriate to

[a]Electronic mail: mcgaughey@cmu.edu

treat them as junctions sandwiched between two bulk leads and to associate the thermal transport through the junction with a thermal conductance. Modeling of thermal transport across solid-solid interfaces and junctions began in the 1950s[20] but was limited to simple analytical models (e.g., the acoustic mismatch and diffuse mismatch models) that could not account for detailed interface geometry.[21] Beginning with Lumpkin *et al.*,[22] a harmonic lattice-based analytical technique was developed that accounted for exact interface atomic postions and interactions. This technique was based on the scattering of incident phonons by the interface,[23,24] was generalized by Zhao and Freund to arbitrary three-dimensional interfaces,[25] and is now known as the scattering boundary method (SBM). Zhao and Freund studied ideal Si-Ge intefaces and verified the validity of the SBM against MD studies of interfaces that used wave packets.[26] Other studies using the SBM focused on the effect of incidence angle on transmission[27] and on the use of non-equilibrium distribution functions in the leads.[28]

The use of non-equilbrium MD (NEMD) simulation to probe interface thermal transport developed in parallel to the SBM. Maiti *et al.* were the first to use NEMD simulation to predict interface thermal conductance, studying grain boundaries in Si.[29] NEMD has since been used to study defective interfaces with LJ and Morse interactions,[30] temperature and disorder effects at LJ interfaces,[31] and Si-Ge interfaces using the Stillinger-Weber potential.[28] Duda *et al.*, using NEMD, noted that the thermal conductance of an isolated LJ interface increased linearly with increasing temperature.[32]

The study of finite-size junctions extended naturally from the techniques developed for isolated interfaces. Landry and McGaughey investigated Si (Ge) thin films sandwiched between bulk Ge (Si) leads. In particular, they studied the dependence of junction thermal conductance on junction length using both SBM calculations and NEMD simulations.[33] Tian *et al.*[34] studied Si-Ge superlattice junctions using a harmonic lattice-based technique,[35,36] where they found that the introduction of disorder at interfaces destroyed coherent transport of phonons, particularly those with high frequencies.

Previous works on superlattices[17,19] and superlattice junctions[16,34] suggest that thermal transport in superlattice junctions depends on both period length and junction length, and is modified by disorder. In this work, we vary both period length and junction length, and consider the effects of lead composition, finite temperature, and disorder. In Section II, we define the structure of the superlattice junction. We describe the three techniques used in Section III: the thermal circuit model, NEMD simulations, and the Landauer transport formula with the SBM. Our findings, notably a lead effect, are reported in Section IV and summarized in Section V.

II. SUPERLATTICE JUNCTION STRUCTURE: THE MULTIPLE THIN FILM SYSTEM

We are interested in calculating the thermal conductance of superlattice junctions with bulk leads. The atoms in our representative crystalline material interact via the pairwise LJ potential with argon parameters. The LJ pairwise interaction is

$$\phi_{ij}(r) = 4\epsilon\left[\left(\frac{\sigma}{r}\right)^{12} - \left(\frac{\sigma}{r}\right)^{6}\right], \tag{1}$$

where r is the distance between any atoms i and j. The argon LJ parameters are $\epsilon = 1.67 \times 10^{-21}$ J and $\sigma = 3.40 \times 10^{-10}$ m. The interaction is cut off at 2.5σ. Two atomic species are used in order to generate the superlattice junction structures: regular argon (Type 1) and "heavy" argon (Type 2). Type 1 and Type 2 atoms interact identically. They differ only in their masses, μ_1 and μ_2. Type 1 argon has the true argon atomic mass, $\mu_1 = 6.634 \times 10^{-26}$ kg. In keeping with previous work on similar systems[7,32] and to capture an atomic mass ratio typical of real nanostructures, $\mu_2 = 3\mu_1$. Thin films of Type 1 and Type 2 atoms are built along the [001] crystallographic direction (i.e., the z axis) in a fashion that alternates between Type 1 and Type 2, as shown in Fig. 1.

The alternating Type 1 and Type 2 thin films form the superlattice junction. A junction is defined by the number of atomic monolayers per thin film n, the number of thin films in the junction m, and the argon face-centered cubic (FCC) conventional unit cell lattice constant a (5.315 Å and 5.370 Å at temperatures of 20 K and 40 K).[37] The length of a single thin film is $na/2$. The length

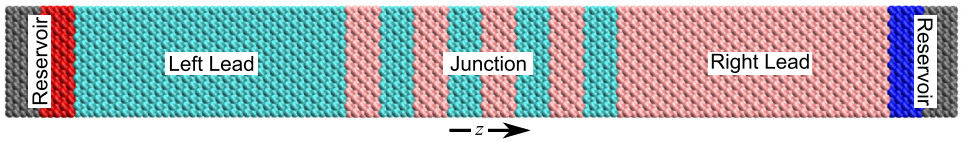

FIG. 1. Example structure for the case of eight thin films ($m = 8$, a mismatched case) with five monolayers per thin film ($n = 5$). Cyan atoms are Type 1 and pink atoms are Type 2. The red and blue atoms are in the reservoirs and the gray atoms are fixed for use in the MD simulations.

of the entire junction is $mna/2$. We discuss cases where $n = \{2, 4, 8\}$ and m ranges from 1 to 40, leading to junction lengths ranging from 1 nm to 40 nm. We do not explore junction lengths greater than 40 nm, as such structures may result in a numerical divergence of the thermal conductance prediction as described by Hu *et al.*[38] Finally, the junction is sandwiched between two bulk-like leads. The left lead is always of Type 1. For m odd, the right lead will be of Type 1 (i.e., matched leads). For m even, the right lead will be of Type 2 (i.e., mismatched leads). m_1 (m_2) are the number of thin films of Type 1 (Type 2) in the junction, such that $m_1 + m_2 = m$. Method-specific details are provided in Sections III B and III C.

III. METHODS

A. Thermal Circuit

If we assume that each Type 1 - Type 2 interface inside a junction acts as a memoryless phonon scatterer and that each constituent thin film has the thermal conductivity equivalent to a bulk of its type, then the junction can be represented by a series of interface and thin film thermal resistors. This assumption leads to a simple but naïve prediction of the junction thermal conductance

$$G_{\mathrm{J,TC}}(T) = \left[\sum_{i=1}^{m_1} \frac{na}{k_1(\overline{T}_i)} + \sum_{j=1}^{m_2} \frac{na}{k_2(\overline{T}_j)} + \sum_{k=1}^{m_1+m_2+1} \frac{1}{G_{\mathrm{Int},1-2}(T_{\mathrm{Int},k})} \right]^{-1}, \tag{2}$$

where k_1 (k_2) is the temperature-dependent bulk crystal thermal conductivity of Type 1 (Type 2) atoms and $G_{\mathrm{Int},1-2}$ is the temperature-dependent per unit area thermal conductance of an isolated Type 1 - Type 2 interface. T is the average temperature of the junction, $\overline{T}_i$ is the average temperature of the i^{th} film within the junction, and $T_{\mathrm{Int},k}$ is the temperature of the k^{th} interface within the junction.

B. Nonequilibrium Molecular Dynamics

The direct heat method[39] in NEMD simulation is performed on the systems of interest using LAMMPS[40] and a time step of 4.34 fs. In an MD simulation, the classical equations of motion are numerically integrated to predict the trajectories of atoms. MD simulations can account for the full effect of the anharmonic interactions between atoms, which is important at finite temperature for LJ interface systems.[32] The aim of the direct heat method is to predict the temperature distribution in the cross-interface (z) direction given a fixed heat flow.

The cross-sectional area of the simulation cell is 6×6 FCC conventional unit cells, giving an area $A = 36a^2$, which is 10.17 nm^2 and 10.38 nm^2 at temperatures of 20 K and 40 K. Each atomic monolayer in the z-direction (i.e., half a conventional unit cell) is composed of $6 \times 6 \times 2 = 72$ atoms. The first four and last four monolayers (288 atoms) of the NEMD system are fixed to prevent atomic sublimation and to give the other atoms a bulk-like environment. Immediately adjacent to both sets of fixed atoms are 16 atomic monolayers (1152 atoms) of thermal reservoir, from which energy will be added or removed during the non-equilibrium portion of the simulation. Interior to the thermal reservoirs on both ends are 120 atomic monolayers (8640 atoms) serving as bulk-like leads.

Velocity rescaling is first performed for 10^6 time steps to ensure that the mean kinetic energy per atom is $1.5k_BT$, where k_B is the Boltzmann constant. The system is then evolved in the microcanonical ensemble for 10^6 time steps to recover realistic Hamiltonian dynamics. For the next 8×10^6 time steps, a fixed amount of energy is removed from the right reservoir and placed in the left reservoir every time step such that total system energy is conserved. This energy transfer is accomplished by rescaling the velocities of the reservoir atoms. Based on the thermal circuit model described in Section III A, the energy transfer (i.e., heat flow) is specifically chosen for the film number, number of monolayers per film, and average temperature of the system so as to produce a cross-junction temperature difference of 5 K. After the 8×10^6 time step run to steady-state, monolayer temperatures and positions are averaged and collected for 5×10^6 time steps. A monolayer's temperature is defined as the temperature corresponding to its mean kinetic energy.

The result of the averaging is a temperature versus position distribution like that shown in Fig. 2 for the case of eight films of eight atomic monolayers each ($m = 8$, $n = 8$) at an average temperature of 20 K. Least-squares linear fits to the temperature profile are performed in the leads. Data in the 40 atomic monolayers closest to either reservoir are not included in the lead fits as their dynamics are influenced by the velocity rescaling. Interface temperatures are defined by extrapolation of the fits to the interface locations and then averaging the values on each side. The thermal conductance of the junction region is obtained from

$$G_{J,NEMD}(T) = \frac{q}{A\Delta T}, \tag{3}$$

where ΔT is the difference between the temperatures of the left lead fit extrapolated to the first interface and the right lead fit extrapolated to the last interface. T is the mean of those two temperatures. As shown in Fig. 2 and in previous work,[8] this method is also able to resolve individual thin film thermal conductivities and intrajunction interface thermal conductances when the thin films are sufficiently large. For systems with eight atomic monolayers per film (e.g., Fig. 2), the resolution is good. For systems with two or four atomic monolayers per film, the resolution is poor.

For a system with eight thin films of eight atomic monolayers each at an average temperature of 20 K, the intrajunction film thermal conductivities are plotted in Fig. 3(a) as a function of the average individual film temperature. These results are compared against temperature-dependent thermal conductivities for bulk Type 1 and Type 2 argon. The film-film thermal interface conductances for the same case are plotted in Fig. 3(b) as a function of interface temperature. The results are compared against the temperature-dependent thermal conductance of an isolated Type 1 - Type 2

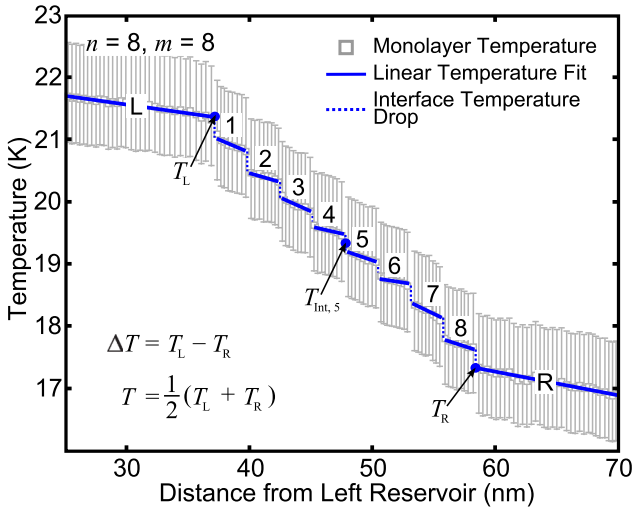

FIG. 2. Temperature profile from NEMD for eight films ($m = 8$) of eight atomic monolayers each ($n = 8$) at an average temperature of 20 K. The error bars on the monolayer temperatures represent their standard deviation over the data collection time steps. The intrajunction films are numbered 1 through 8, while the left and right leads are labeled L and R.

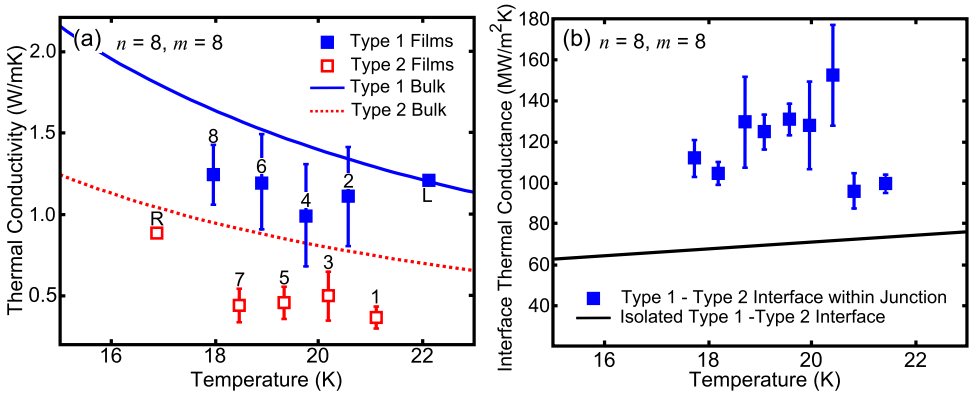

FIG. 3. Intrajunction (a) film thermal conductivities and (b) film-film interface thermal conductances for the same case as Fig. 2 ($n = 8$, $m = 8$). These data are averaged from temperature profiles from five independent NEMD runs, including the profile shown in Fig. 2. They are compared against temperature-dependent NEMD values of bulk thermal conductivity and isolated interface thermal conductance. The error bars indicate the standard deviation over the five independent runs.

interface. The bulk thermal conductivities and isolated interface thermal conductances are obtained from independent NEMD simulations.

The decrease of thermal conductivity inside the thin films [points 1 through 8 in Fig. 3(a)] compared to bulk is consistent with the memoryless interface scattering assumption of the thermal circuit model, where complete carrier scattering at the interfaces causes a reduction of their mean free paths. Note that for the long leads [points L and R in Fig. 3(a)], no such reduction is present and the thermal conductivity predictions are close to the bulk values. The 50 to 100% increase of the film-film interface thermal conductances [Fig. 3(b)], however, is not consistent with the assumption of memoryless interface scattering. A possible cause of the elevation in thermal conductance is the emergent periodicity of the superlattice junction. The periodicity causes interference between vibrational waves that are scattered by the regularly-spaced interfaces. This effect may be masked within MD simulations due to anharmonic scattering, so we will use a harmonic, lattice-based technique for further analysis.

C. Scattering Boundary Method

1. Landauer formula

To isolate the effects of the emergent periodicity, we now limit our analysis to harmonic interactions and consider the transport of vibrational mode energy across the junction. Despite the advantages described in Section III B, MD simulations do not provide information about the vibrational modes of the system without additional, computationally-expensive processing steps.[7,41,42] In order to extract mode-level detail, we move to a method built explicitly upon the basis of vibrational modes. Consider a model where the vibrational modes of the left lead are coupled to vibrational modes of the right lead via the junction. Since the leads are bulk crystals, their vibrational modes are phonon modes. Further, because there is no anharmonic scattering, the transport through the junction is ballistic and the transmission is elastic (i.e., there is no coupling between vibrational modes of different frequency). Finally, we assume that the temperature difference between the left and right leads is infinitesimal. These conditions and assumptions allow us to apply the Landauer ballistic transport formula to compute the thermal conductance of our superlattice junctions.[43]

In the classical limit, application of this formula results in the following expression for the junction thermal conductance

$$G_{\mathrm{J,SBM}} = \frac{1}{V} \sum_{\boldsymbol{\kappa},\nu}^{\mathrm{Left},+z} k_{\mathrm{B}}\, v^{\mathrm{I}}_{g,z}(\boldsymbol{\kappa},\nu)\, \alpha_{\mathrm{L}\to\mathrm{R}}(\boldsymbol{\kappa},\nu). \tag{4}$$

The summation is performed over all rightward traveling bulk phonon modes of the left lead (i.e., incident phonon modes), with each phonon mode being described by a wavevector $\boldsymbol{\kappa}$ and a polarization ν. V is the volume per mode in the reciprocal space of the left lead crystal. $v_{g,z}^{\mathrm{I}}$ is the z-component of the group velocity of the incident phonon mode (I indicates incident). Determination of the bulk phonon properties is done via harmonic lattice dynamics calculations.[44] The junction coupling comes in via the transmission coefficient $\alpha_{\mathrm{L}\to\mathrm{R}}$, a mode-dependent dimensionless quantity that takes on values between zero and unity. In the particle picture, α is the fraction of phonon energy quanta that cross the junction given an incident flux. In the wave picture, α is the fraction of energy flux from the incident wave that crosses the junction.

We use the SBM to compute the transmission coefficients of the incident phonon modes.[23,25,27,28] The SBM is comprised of two steps, which are briefly described in Sections III C 2 and III C 3. For a detailed derivation, please see Wang and Wang[27] or Zhao and Freund.[25] For each junction, bulk phonon properties and phonon transmission coefficients are calculated for rightward traveling modes at 10,000 wavevectors uniformly sampled from the first Brillouin zone of the left lead. Thermal conductance is computed by performing a summation over the sampled modes as shown in Eq. (4). We validate our implementation of the SBM against a zero temperature extrapolation of the isolated Type 1 - Type 2 interface thermal conductances from our NEMD simulations [the black line in Fig. 3(b)]. The difference between the SBM calculation and the NEMD extrapolation is 8%. Our NEMD interface thermal conductances and extrapolation agree well with results from Duda *et al.*[32]

2. Determination of scattered modes

When phonons of wavevector and polarization $[\boldsymbol{\kappa},\nu]^{\mathrm{I}}$ encounter the junction, some of the energy is reflected back into the left lead, while the remainder is transmitted into the right lead. The first part of the procedure to compute $\alpha_{\mathrm{L}\to\mathrm{R}}([\boldsymbol{\kappa},\nu]^{\mathrm{I}})$ is to determine what modes are excited in reflection and what modes are excited in transmission. Let the set of possible reflected modes be denoted by $[\boldsymbol{\kappa},\nu]_j^{\mathrm{R}}$ and the set of possible transmitted modes be denoted by $[\boldsymbol{\kappa},\nu]_i^{\mathrm{T}}$, where indices i and j indicate that there may be many such modes. Due to the identical crystal structures and lattice constants of Type 1 and Type 2 argon, periodicity in the x-y plane is preserved, hence the x and y components of $\boldsymbol{\kappa}_j^{\mathrm{R}}$ and $\boldsymbol{\kappa}_i^{\mathrm{T}}$ must equal those of the incident mode. The conservation of the wavevector in the x-y plane is equivalent to assuming totally specular scattering. Due to the assumption of elastic transmission, the frequency of the reflected and transmitted modes are identical to that of the incident mode. The problem of finding all phonon modes in both the left and right leads that have the same κ_x, κ_y, and ω as the incident mode can be formulated and solved as a generalized eigenvalue problem.

3. Scattering boundary equations

Once the reflected and transmitted mode sets $[\boldsymbol{\kappa},\nu]_j^{\mathrm{R}}$ and $[\boldsymbol{\kappa},\nu]_i^{\mathrm{T}}$ have been determined, $\alpha_{\mathrm{L}\to\mathrm{R}}$ $([\boldsymbol{\kappa},\nu]^{\mathrm{I}})$ can be computed by solving the equations of motion of the junction atoms and the lead atoms in the vicinity of the junction. The Newtonian equations of motion are written down explicitly for each junction atom, including interactions with junction atoms and lead atoms. Two equations are written down for each lead atom. The first equation is its Newtonian equation of motion. The second equation is one that enforces the motion of the lead atom as a superposition of incident and reflected modes (for the left side) or transmitted modes (for the right side). These modes have unknown amplitudes R_j and T_i. The assumption of elastic scattering allows us to ascribe an identical periodic time-evolution of $\exp(i\omega t)$ to each atom. The specification of this evolution converts the system of linear differential equations into a system of linear algebraic equations. The identical periodic time evolution means the SBM solutions are time coherent.

This overdetermined system of equations is solved by minimizing the squared error using singular value decomposition. Finally, the modal transmission coefficient is determined as

$$\alpha_{\mathrm{L}\to\mathrm{R}}(\boldsymbol{\kappa},\nu) = \sum_i \frac{v_{g,z}^{\mathrm{I}}}{v_{g,i,z}^{\mathrm{T}}}|T_i|^2, \tag{5}$$

where the summation is performed over all transmitted modes. $v^{\mathrm{T}}_{g,i,z}$ is the z-component of the group velocity of the i^{th} transmitted mode.

IV. RESULTS

A. NEMD Indicates a Lead Effect

The length dependence of the thermal conductance for superlattice junctions with two, four, and eight atomic monolayers per thin film at average temperatures of 20 K and 40 K were extracted from NEMD simulations. Values for each case were determined as an average over five independent simulations. A select subset of the results are plotted in Figs. 4(a)-4(d). Power law fits for even thin film number and odd thin film number junctions are also plotted, as is the thermal conductance predicted from the thermal circuit model for the same configurations [Eq. (2)]. In all cases, the thermal circuit model underpredicts the NEMD result. The average underprediction throughout the length domain as a percentage of the thermal circuit conductance for two atomic monolayers per film is 60% at 20 K and 26% at 40 K. For four atomic monolayers per film, the underprediction is 34% at 20 K and 9% at 40 K. For eight atomic monolayers per film, the underprediction is 16% at 20 K and 11% at 40 K. This consistent underprediction indicates that the assumption of diffusive transport within films and memoryless scattering at the intrajunction interfaces in the thermal circuit model is an incomplete description of the energy transport process. The discrepancy is largest at low temperature and small film thickness [Fig. 4(a)], while the high temperature [Fig. 4(b)] and large film thickness [Fig. 4(c)] NEMD results are closer to the thermal circuit predictions. The latter results are not surprising since diffusive transport becomes dominant in the high temperature and large film thickness limits. The data in Fig. 4(d) are for cases where species disorder is introduced at the lead-junction and intrajunction interfaces.[45]

The power law fits are used to differentiate between cases where the thin film number is odd and the leads are of the same type (matched) and cases where the thin film number is even and

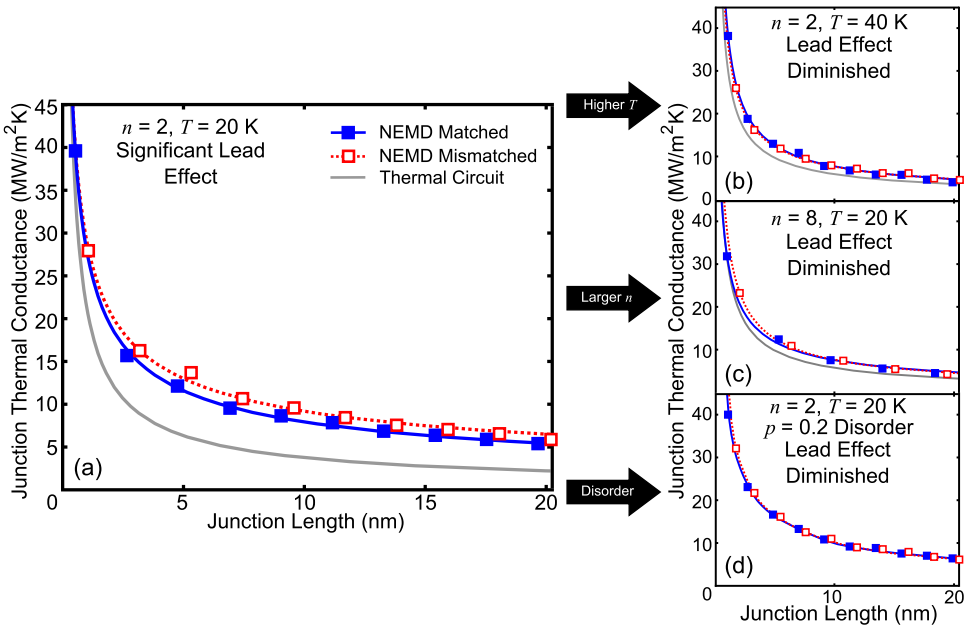

FIG. 4. Length-dependent junction thermal conductances for the cases (a) $n = 2$, $T = 20$ K, (b) $n = 2$, $T = 40$ K, (c) $n = 8$, $T = 20$ K, and (d) $n = 2$, $T = 20$ K with $p = 0.2$ interfacial species disorder from NEMD and the thermal circuit model. The $n = 2$, $T = 20$ K case shows a strong lead effect, which persists as the number of junction thin films increases. The lead effect is diminished at higher temperatures, greater number of monolayers per thin film, and with the introduction of species disorder at the interfaces.

the leads are of differing type (mismatched). We observe for both temperatures and at all thin film thicknesses that the junction thermal conductances of the mismatched cases are elevated compared to the matched cases at similar lengths. Since the mismatched and matched cases are always at different lengths, it is more appropriate to compare the power law fits. In most of the configurations presented, the difference between the matched and mismatched cases is within the uncertainty of the fits. A clear difference in trend, however, can be observed for the case of two atomic monolayers per film at a temperature of 20 K [Fig. 4(a)]. In this case, the 95% confidence intervals of the power law fits (which, for the sake of clarity, are not shown) share very small overlap and the difference between the trends is statistically significant. The mismatched cases consistently exhibit a thermal conductance that is 10% higher than the matched cases at comparable length. In the thermal circuit model, matched and mismatched cases differ only in an additional interface resistance. This difference goes to zero in the limit of large junction size, as the resistance of a single interface becomes negligible compared to the overall resistance of the junction. The 10% difference in conductance seen in the NEMD results, however, persists at all examined lengths with no noticeable attenuation up to the longest lengths investigated. Further NEMD simulations for the $n = 2$ case were performed at average junction temperatures of 15, 10, and 5 K.[46] The same lead effect persists at all temperatures investigated. In conjunction with the elevation of intrajunction interface thermal conductances discussed in Section III B [Fig. 3(b)], the lead effect provides further evidence that the thermal circuit model is insufficient.

The lead effect diminishes when (i) temperature is increased [Fig. 4(b)], (ii) the intrajunction thin films are made thicker [Fig. 4(c)], and (iii) species disorder is introduced to the lead-junction and intrajunction interfaces [Fig. 4(d)]. The increase of temperature increases anharmonic scattering, leading to diffusive transport. Hence, one hypothesis is that the lead effect is caused by partial ballistic transport of energy carriers across the junction. These carriers are not bulk phonons of the constituent films, but rather emergent modes of the superlattice junction. Much like phonons of bulk superlattices,[7] these modes do not consider the intrajunction interfaces as defects and do not scatter from them. Disorder at the intrajunction interfaces, however, does act as a scattering source for these emergent modes. Hence, in agreement with earlier work,[34] the introduction of species disorder at interfaces also leads to diffusive transport.

If the lead effect is completely attributable to ballistic transport, we would expect saturation of both matched and mismatched junction thermal conductances to a single, fully diffusive limit at long junction lengths (as is the case with thin films of bulk crystals).[33] For the junction lengths evaluated, however, this saturation is not observed. Instead, the lead effect diminishes as the length of the junction's constituent thin films is increased [Fig. 4(c)], not as the total junction length is increased. Within a single thin film, this result can be explained as a size effect related to the thin film length and the mean free paths of the phonons of the film's constituent material.[33] In the picture of the emergent superlattice modes, however, increasing the superlattice period alters the modes themselves.[7] It is known that the thermal conductivity of a bulk superlattice is sensitive to its period (i.e., the minimum in superlattice thermal conductivity) and can be partitioned into a regime where vibrational wave interference is significant and one where interference is not.[17,19] Hence, another hypothesis is that the lead effect is partially attributable to vibrational wave interference in the superlattice junction. Increasing the period of the superlattice junction attenuates the lead effect by moving the system out of the regime where interference is significant.

B. Lead Effect is Reversed in Harmonic Calculation

The interesting case of two atomic monolayers per film at a temperature of 20 K is now analyzed using the SBM. As discussed in Section III C 3, the fully harmonic nature of the SBM calculation has two consequences. First, it considers transport that is completely ballistic. Second, any spatial interference effects caused by the emergent superperiodicity of the junction are preserved. Hence, the SBM can be used to evaluate the two hypotheses posed at the end of Section IV A.

Since classical statistics are used to achieve parity with the MD simulations, the only finite temperature effect in the SBM is the setting of the lattice constant equal to the equilibrium value

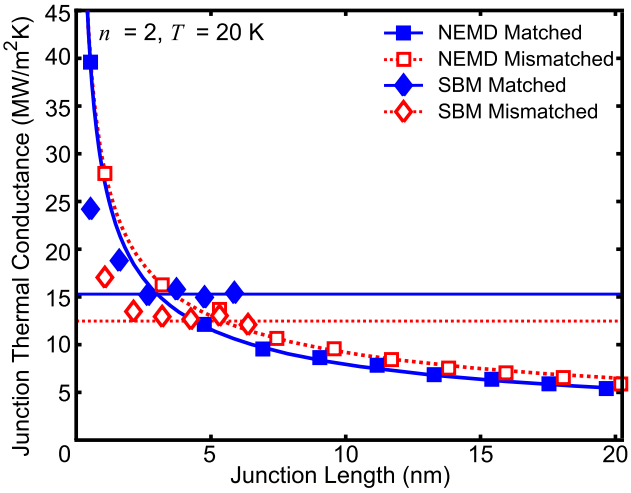

FIG. 5. Length-dependent junction thermal conductances for the case $n = 2$, $T = 20$ K from NEMD simulations and the SBM calculations. Red and blue curves under the square symbols are power law fits to the NEMD data. Red and blue lines under the diamond symbols are the length-converged SBM results.

at a temperature of 20 K. As plotted in Fig. 5, the SBM junction thermal conductances converge to length-independent values at a junction length of approximately 4 nm. These results stand in contrast to the NEMD results, where scattering within the junction causes the junction thermal conductances to continue to decrease with increasing junction length. While the SBM results are length-independent beyond junction lengths of 4 nm, they exhibit a strong dependence on the lead properties (i.e., matched or mismatched) at all lengths. The cases with matched leads converge to a junction thermal conductance of 16 MW/m^{2}K, while the cases with mismatched leads converge to 13 MW/m^{2}K, a difference of 19%. The SBM captures the lead effect, but the relative magnitudes of the matched versus mismatched junction thermal conductances are flipped when compared to the NEMD results.

The origin of the lead effect in the SBM calculations can be revealed by examining the transmission coefficients plotted in Figs. 6(a) and 6(b). Fig. 6(a) corresponds to a matched case with seven junction thin films (3.7 nm), while Fig. 6(b) corresponds to a mismatched case with eight junction thin films (4.2 nm). Since the thermal conductances for both cases have converged with junction length (Fig. 5), the differences in their transmission coefficients must be due to the differing

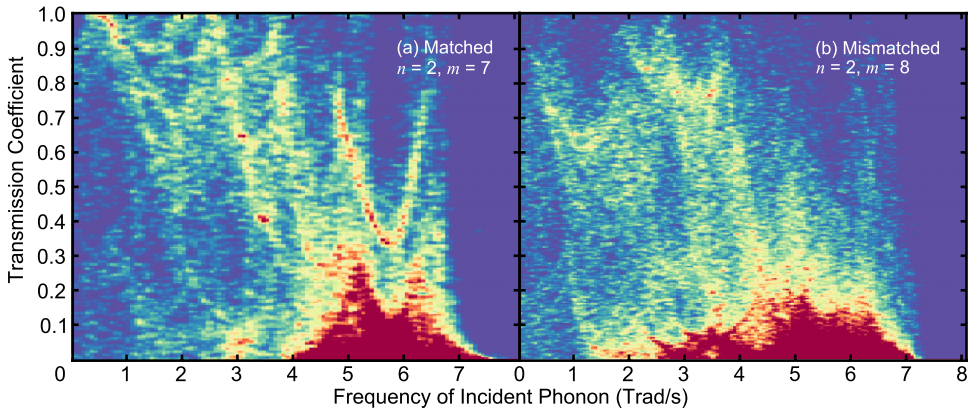

FIG. 6. Transmission coefficient versus frequency color histograms from the SBM for length-converged matched and mismatched cases. Since these results represent length-converged systems, differences in transmission coefficients between the two cases are due to differences in the right lead mass. The cutoff frequency of Type 2 argon is 7.23 Trad/s. Different colors represent the number of modes in bins of frequency and transmission coefficient.

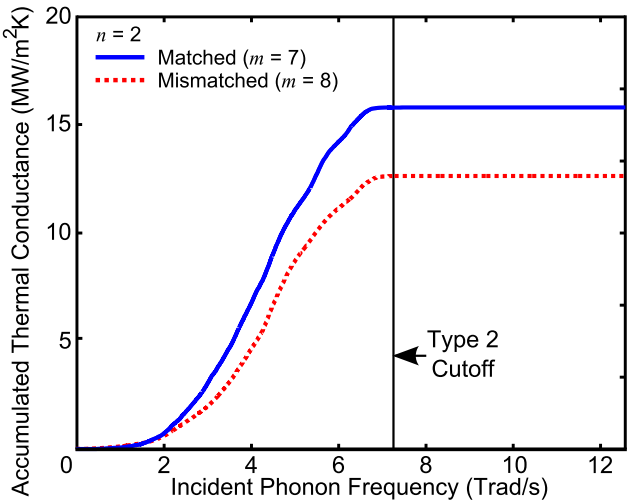

FIG. 7. Accumulation of junction thermal conductance with frequency from the SBM for length-converged matched and mismatched cases.

mass of the right lead. The lead effect is not due to the lower cutoff frequency of the Type 2 material, but instead due to details in the shared frequency range of the two materials. While the mismatched case has exactly zero transmission for incident phonons of frequency greater than the Type 2 cutoff, the matched case shows only small transmission beyond the Type 2 cutoff. This finding is highlighted in Fig. 7, where the accumulation of the junction thermal conductance against incident phonon frequency is plotted for both matched and mismatched cases. For the matched case, incident phonons above the Type 2 cutoff frequency result in only 0.7% of the overall thermal conductance. Instead, the difference in thermal conductance can be attributed to dips in the transmission coefficients that appear at 1 and 3 Trad/s in Fig. 6(b), but are far less significant in Fig. 6(a). The difference can also be attributed to slower accumulation of the thermal conductance between 2-3 and 5-6 Trad/s. We attribute the maxima and minima in the transmission coefficients seen in Figs. 6(a) and 6(b) to constructive and destructive interference between reflections and transmissions across successive intrajunction interfaces.

V. SUMMARY

Our investigation of superlattice junctions reveals that their thermal conductance at finite temperature depends on the material properties of the leads. Specifically, systems with mass-mismatched leads have higher thermal conductance than those with mass-matched leads. This dependence persists when overall junction length is increased [Fig. 4(a)], but diminishes when temperature is increased [Fig. 4(b)], when the thicknesses of the constituent films are increased [Fig. 4(c)], and when species disorder is introduced at the lead-junction and intrajunction interfaces [Fig. 4(d)].

We partially attribute the lead effect to ballistic transport of emergent modes of the superlattice junction. These modes travel ballistically across the junction and do not scatter from the intrajunction interfaces. Increasing temperature and the introduction of species defects at interfaces cause these emergent modes to scatter with one another and with the defects, resulting in attenuation of the lead effect. Increasing the superlattice period of the junction likewise attenuates the lead effect, suggesting that the effect can also be attributed to vibrational wave interference within the junction. The dependence of the lead effect on the superlattice period may be similar to the transition between coherent and incoherent regimes in a bulk superlattice.

As evidenced by the SBM calculations, the lead effect is also present in the zero temperature, harmonic limit (Fig. 5), but it is reversed. In this limit, the phonon transmission coefficients (and consequentially the thermal conductances) are highly dependent on the right lead mass (Fig. 6). It

is not surprising that the lead effect can be altered by the introduction of finite temperature (and along with it, anharmonic interactions). It is surprising, however, that the effect of finite temperature is not simply to reduce the lead effect until none can be observed. Instead, the reversal of the lead effect when comparing the SBM data to the NEMD data (Fig. 5) suggests the existence of a regime where finite temperature affects the matched and mismatched cases differently. In this intermediate regime, the effect of finite temperature appears to drive the junction thermal conductance of the matched case higher than that of the mismatched case. As discussed in Section IV A, we performed NEMD simulations at average junction temperatures as low as 5 K for the case of $n = 2$ in an attempt to access this regime. We observed the same lead effect as at 20 K in all cases and did not notice any evidence of an appreciable attenuation or reversal. While direct heat method NEMD simulation does not provide concrete evidence of the reversal of the lead effect, the existence of the intermediate regime could be probed by modal anharmonic analysis of matched and mismatched cases in the temperature range of 0 to 5 K.[47–49]

ACKNOWLEDGMENTS

This work was supported by NSF Award DMR1006480. We thank Michael Widom (Carnegie Mellon University), Baowen Li (National University of Singapore), and Kimmo Sääskilahti (Aalto University) for insightful discussion.

[1] A. Y. Cho, Appl. Phys. Lett. **19**, 467 (1971).
[2] L. Esake and L. L. Chang, Phys. Rev. Lett. **31**, 2080 (1974).
[3] T. Yao, Appl. Phys. Lett. **51**, 1798 (1987).
[4] G. Chen, A. Verma, and J. S. Smith, Appl. Phys. Lett. **67**, 3554 (1995).
[5] S. M. Lee, D. G. Cahill, and R. Venkatasubramanian, Appl. Phys. Lett. **70**, 2957 (1997).
[6] E. S. Landry, M. I. Hussein, and A. J. H. McGaughey, Phys. Rev. B **77**, 184302 (2008).
[7] S. C. Huberman, J. M. Larkin, A. J. H. McGaughey, and C. H. Amon, Phys. Rev. B **88**, 155311 (2013).
[8] E. S. Landry and A. J. H. McGaughey, Phys. Rev. B **79**, 075316 (2009).
[9] K. Imamura, Y. Tanaka, N. Nishiguchi, S. Tamura, and H. J. Maris, J. Phys.: Condens. Matter **15**, 8679 (2003).
[10] K. Termentzidis, P. Chantrenne, and P. Keblinski, Phys. Rev. B **79**, 214307 (2009).
[11] Y. Chen, D. Li, J. R. Lukes, Z. Ni, and M. Chen, Phys. Rev. B **72**, 174302 (2005).
[12] T. Zhu and E. Ertekin, Phys. Rev. B **90**, 195209 (2014).
[13] N. Yang, G. Zhang, and B. Li, Nano Lett. **8**, 276 (2008).
[14] I. Savic, D. Donadio, F. Gygi, and G. Galli, Appl. Phys. Lett. **102**, 073113 (2013).
[15] J. Garg, N. Bonini, and N. Marzari, Nano Lett. **11**, 5135 (2011).
[16] M. N. Luckyanova, J. Garg, K. Esfarjani, A. Jandi, M. T. Bulsara, A. J. Schmidt, A. J. Minnich, S. Chen, M. S. Dresselhaus, Z. Ren *et al.*, Science **338**, 936 (2012).
[17] M. V. Simkin and G. D. Mahan, Phys. Rev. Lett. **84**, 927 (2000).
[18] J. Jiang, J. Wang, and B. Wang, Appl. Phys. Lett. **99**, 043109 (2011).
[19] J. Ravichandran, A. K. Yadav, R. Cheaito, P. B. Rossen, A. Soukiassian, S. J. Suresha, J. C. Duda, B. M. Foley, C.-H. Lee, Y. Zhu *et al.*, Nat. Mater. **13**, 168 (2014).
[20] W. A. Little, Can. J. Phys. **37**, 334 (1959).
[21] E. T. Swartz and R. O. Pohl, Rev. Mod. Phys. **61**, 605 (1989).
[22] M. E. Lumpkin, W. M. Saslow, and W. M. Visscher, Phys. Rev. B **17**, 4295 (1978).
[23] D. A. Young and H. J. Maris, Phys. Rev. B **40**, 3685 (1989).
[24] S. Pettersson and G. D. Mahan, Phys. Rev. B **42**, 7386 (1990).
[25] H. Zhao and J. B. Freund, J. Appl. Phys. **97**, 024903 (2005).
[26] P. K. Schelling, S. R. Phillpot, and P. Keblinski, Appl. Phys. Lett. **80**, 2484 (2003).
[27] J. Wang and J.-S. Wang, J. Phys.: Condens. Matter **19**, 236211 (2007).
[28] E. S. Landry and A. J. H. McGaughey, Phys. Rev. B **80**, 165304 (2009).
[29] A. Maiti, G. D. Mahan, and S. T. Pantelides, Solid State Commun. **102**, 517 (1997).
[30] C. J. Twu and J. R. Ho, Phys. Rev. B **67**, 205422 (2003).
[31] R. J. Stevens, L. V. Zhigilei, and P. M. Norris, Int. J. Heat Mass Transfer **50**, 3977 (2007).
[32] J. C. Duda, T. S. English, E. S. Piekos, W. A. Soffa, L. V. Zhigilei, and P. E. Hopkins, Phys. Rev. B **84**, 193301 (2011).
[33] E. S. Landry and A. J. H. McGaughey, J. Appl. Phys. **107**, 013521 (2010).
[34] Z. Tian, K. Esfarjani, and G. Chen, Phys. Rev. B **89**, 235307 (2014).
[35] H. Zhao and J. B. Freund, J. Appl. Phys. **105**, 013515 (2009).
[36] J.-S. Wang, J. Wang, and J. T. Lü, Eur. Phys. J. B **62**, 381 (2008).
[37] A. J. H. McGaughey, Ph.D. thesis, University of Michigan, Ann Arbor (2004).
[38] L. Hu, W. J. Evans, and P. Keblinski, J. Appl. Phys. **110**, 113511 (2011).
[39] P. K. Schelling, S. R. Phillpot, and P. Keblinski, Phys. Rev. B **65**, 144306 (2002).
[40] S. Plimpton, J. Comp. Phys. **117**, 1 (1995).
[41] A. J. H. McGaughey and M. Kaviany, Phys. Rev. B **71**, 184305 (2005).

[42] K. Sääskilahti, J. Oksanen, J. Tulkki, and S. Volz, Phys. Rev. B **90**, 134312 (2014).
[43] R. Landauer, Philos. Mag. **21**, 863 (1970).
[44] M. T. Dove, *Introduction to Lattice Dynamics* (Cambridge University Press, 2005).
[45] Disorder at the interface is introduced in this fashion: atoms within a thin film of Type 1 (Type 2) immediately adjacent to an interface have a probability p of being Type 2 (Type 1). No comparisons to the thermal circuit model are made for the disordered cases.
[46] The conventional unit cell lattice constants of LJ argon at 5, 10, and 15 K are 5.280 Å, 5.289 Å, and 5.303 Å. These values are interpolated from data presented in Ref. 37.
[47] K. Sääskilahti, J. Oksanen, J. Tulkki, and S. Volz, Phys. Rev. B **90**, 134312 (2014).
[48] Y. Chalopin, N. Mingo, J. Diao, D. Srivastava, and S. Volz, Appl. Phys. Lett. **101**, 221903 (2012).
[49] Y. Chalopin and S. Volz, Appl. Phys. Lett. **103**, 051602 (2014).